

1 **Oxygen and hydrogen ion abundance in the**
2 **near-Earth magnetosphere: Statistical results on the**
3 **response to the geomagnetic and solar wind activity**
4 **conditions**

E. A. Kronberg¹, S. E. Haaland^{1,2}, P. W. Daly¹, E. E. Grigorenko³, L. M.

Kistler⁴, M. Fränz¹, and I. Dandouras⁵

E. A. Kronberg, Max-Planck Institute for Solar System Research, Katlenburg-Lindau, Germany (kronberg@mps.mpg.de)

S. E. Haaland, Max-Planck Institute for Solar System Research, Katlenburg-Lindau, Germany. Also at Department of Physics and Technology, University of Bergen, Norway. (stein.haaland@ift.uib.no)

P. W. Daly, Max-Planck Institute for Solar System Research, Katlenburg-Lindau, Germany (daly@mps.mpg.de)

E. E. Grigorenko, Space Research Institute, Russian Academy of Sciences, Moscow, Russia (elenagrigorenko2003@yahoo.com)

L. M. Kistler, University of New Hampshire, Durham, NH, USA (Lynn.Kistler@unh.edu)

M. Fränz, Max-Planck Institute for Solar System Research, Katlenburg-Lindau, Germany (fraenz@mps.mpg.de)

I. Dandouras, IRAP, University of Toulouse, UPS-OMP, CNRS, Toulouse, France (Iannis.Dandouras@irap.omp.eu)

5 **Abstract.** The composition of ions plays a crucial role for the fundamen-
6 tal plasma properties in the terrestrial magnetosphere. We investigate the
7 oxygen-to-hydrogen ratio in the near-Earth magnetosphere from $-10 R_E <$
8 $X_{GSE} < 10 R_E$. The results are based on seven years of ion flux measure-
9 ments in the energy range ~ 10 keV to ~ 955 keV from the RAPID and CIS
10 instruments on board the Cluster satellites. We find that (1) hydrogen ions
11 at ~ 10 keV show only a slight correlation with the geomagnetic conditions
12 and interplanetary magnetic field changes. They are best correlated with the
13 solar wind dynamic pressure and density, which is an expected effect of the
14 magnetospheric compression; (2) ~ 10 keV O^+ ion intensities are more strongly

¹Max Planck Institute for Solar System

Research, Katlenburg-Lindau, Germany

²Department of Physics and Technology,

University of Bergen, Norway

³Space Research Institute, Russian

Academy of Sciences, Moscow, Russia

⁴University of New Hampshire, Durham,

NH, USA

⁵Institut de Recherche en Astrophysique

et Planétologie, University of Toulouse,

UPS-OMP, CNRS, Toulouse, France

15 affected during disturbed phase of a geomagnetic storm or substorm than
16 >274 keV O^+ ion intensities, relative to the corresponding hydrogen inten-
17 sities; (3) In contrast to ~ 10 keV ions, the >274 keV O^+ ions show the strongest
18 acceleration during growth phase and not during the expansion phase itself.
19 This suggests a connection between the energy input to the magnetosphere
20 and the effective energization of energetic ions during growth phase; (4) The
21 ratio between quiet and disturbed times for the intensities of ion ionospheric
22 outflow is similar to those observed in the near-Earth magnetosphere at >274
23 keV. Therefore, the increase of the energetic ion intensity during disturbed
24 time is more likely due to the intensification than to the more effective ac-
25 celeration of the ionospheric source. In conclusion, the energization process
26 in the near-Earth magnetosphere is mass dependent and it is more effective
27 for the heavier ions.

1. Introduction

28 There are two major sources for the ion population in Earth's magnetosphere: the solar
29 wind and the ionosphere.

30 Hydrogen, helium and oxygen are the most abundant elements in the solar wind. Ac-
31 cording to measurements by SWICS on Ulysses, the oxygen abundance (H/O ratio) varies
32 significantly between fast and slow solar winds, with mean values of 1500 and 2300, re-
33 spectively [e.g., *von Steiger et al.*, 2010]. A direct entry of solar wind plasma into the
34 magnetosphere is believed to occur mainly when the interplanetary magnetic field (IMF)
35 is oriented southward. This leads to reconnection first at the dayside magnetopause and
36 then in the magnetotail. Also, northward IMF results in reconnection at southern and
37 northern high latitudes, facilitating the entry of solar wind plasma.

38 The main source of oxygen in the magnetosphere is believed to be the terrestrial iono-
39 sphere [*Yau et al.*, 1984; *Lockwood et al.*, 1985; *Gloeckler et al.*, 1985; *Chappell et al.*,
40 1987; *Yau and Andre*, 1997; *Chappell et al.*, 2000; *Cully et al.*, 2003b; *Huddleston et al.*,
41 2005; *Moore and Horwitz*, 2007; *Kitamura et al.*, 2010], where oxygen ions are accelerated
42 upward by electric fields parallel to the background magnetic field and pressure gradients.
43 The ionospheric ions are either accelerated in the cusp/cleft region and then convected
44 across the polar cap into the lobe [*Lockwood et al.*, 1985; *Kistler et al.*, 2010], or they
45 come from the nightside aurora, which provides a fast feeding of O^+ ions in the near-
46 Earth plasma sheet during the substorm expansion phase [*Yau et al.*, 1985; *Daglis and*
47 *Axford*, 1996]. The kinetic energy of upflowing ions is typically a few tens of eV [*Yau*
48 *and Andre*, 1997], whereas typical plasma sheet energies are much higher [e.g., *Lennarts-*

49 *son and Shelley*, 1986]. Centrifugal forces accelerate particles as they travel tailward
50 along field lines [e.g., *Cladis*, 1986; *Nilsson et al.*, 2008, 2010], but the most significant
51 energization will take place after the particles enter the plasma sheet.

52 The accelerated plasma sheet particles are convected Earthward and populate the ring
53 current which influences the transport in the radiation belts. The radiation belts are a key
54 region for space weather studies, as their dynamics can induce damage to satellites and
55 other space weather effects. Forecasting models based on radiation belt dynamics include
56 the dynamics of the ring current. Additional ionospheric particles affect the background
57 magnetic field, densities, temperature and convection electric field, and therefore lead to,
58 e.g., changes in the ring current [*Welling et al.*, 2011]. It is challenging to include the
59 heavy ion contribution in numerical studies of the ring current [e.g., *Glocer et al.*, 2009;
60 *Welling et al.*, 2011] or radiation belt models. Knowledge about the ion composition and
61 its dependence on solar wind and magnetospheric conditions is important for defining the
62 boundary conditions in such simulations.

63 A number of earlier studies have demonstrated that the abundance of oxygen in the ring
64 current region can change significantly with geomagnetic activity. *Sharp et al.* [1981] have
65 reported measurements of oxygen in the energy range 0–17 keV/e at distances between
66 11 and 23 R_E downtail by the ISEE 1 spacecraft. *Gloeckler et al.* [1985] analyzed for the
67 first time the ion composition measurements of the ring current during the storm time
68 using AMPTE/CCE spacecraft data in the energy range ~ 1 to 300 keV/e at L values
69 between ~ 3 and 6.5. They suggested that large changes in the O^+ number and energy
70 densities implied an injection of energetic ionospheric ions. *Hamilton et al.* [1988], using
71 AMPTE particle measurements, found an event in which the O^+ dominates H^+ in the ring

72 current during a large magnetic storm. A later study by *Daglis et al.* [2000] established a
73 connection between O^+ (50-426 keV, measured by CRRES) enhancements during storms
74 and substorm activities in the inner magnetosphere at $L \sim 7$. Another, more extensive
75 study by *Fu et al.* [2002], using CRRES observations, has shown that not all injection
76 events have the same ion composition. Their statistical results demonstrated that about
77 73% of all the events were rich in oxygen ions and the rest have very low admixtures
78 of oxygen. Events without oxygen ions were found to be mainly correlated with weak
79 geomagnetic activity conditions.

80 The abundance of oxygen in the magnetotail's plasma sheet can vary significantly with
81 geomagnetic activity. *Moebius et al.* [1987] showed that the spectra harden in the mag-
82 netotail's plasma sheet during substorm, with a larger energy increase for O^+ than for
83 H^+ , i.e., the O^+/H^+ ratio also increases with energy. For this case study they used ob-
84 servations from AMPTE/IRM which resolved the ion composition of the suprathermal
85 population (10-230 keV/e). *Kistler et al.* [1990] used AMPTE/IRM observations to com-
86 pare spectral changes at 15–19 R_E (tail) and 7–9 R_E (inner magnetosphere, night side).
87 They found that the spectral changes were very similar at both locations. *Kistler et al.*
88 [1994] investigated how the flux of the energetic particles observed by the AMPTE/IRM
89 decreases after the initial particle “injection”. These observations show that the decay
90 rate is organized by total energy, energy per charge and velocity. In a statistical study,
91 *Nosé et al.* [2009] used 16 years of Geotail data in order to look at the suprathermal ion
92 composition in the plasma sheet in the range $-100R_E < X_{GSM} < -8R_E$. They investi-
93 gated the correlation between the O^+/H^+ ratio and solar activity using the F10.7 index
94 and with the geomagnetic activity using the Kp index. They found that physical pro-

cesses in the plasma sheet are expected to be much different during solar minimum and
solar maximum, because the Alfvén velocity changes significantly between these two solar
activity regimes. More recently, ion composition data from the CIS/CODIF instrument
on the Cluster spacecraft were used to study O^+ and H^+ bulk content (0–40 keV/e) in
the plasma sheet within 15–19 R_E as a function of solar activity and geomagnetic activity
[Mouikis *et al.*, 2010]. They found that the O^+ density were strongly dependent on these
parameters.

In this paper, we present a comprehensive study of the O^+ and H^+ abundance in the
plasma sheet of the near-Earth magnetosphere (from $-10 R_E < X_{GSE} < 10 R_E$). The
data are obtained from seven years of particle measurements by the Cluster satellites.
We compare the characteristic behavior of the ions at ~ 10 keV and at 274–955 keV to
different solar wind and geospace activity factors.

The novelty of this study is a combination of (a) the extensive spatial region coverage of
the near-Earth magnetosphere, (many previous studies either focused on the magnetotail
region or were mainly case studies in the near-Earth region only); (b) energy range, as
no extensive statistical study has been done so far with energies up to ~ 955 keV; (c)
a comparative analysis of ion intensities at different energies, namely at ~ 10 keV and
from 274 keV to ~ 955 keV; (d) the advantage of having more accurate parameters of the
solar-terrestrial coupling which became available during the last 15 years.

We can for the first time investigate the details of how the near-Earth hydrogen and
oxygen populations depend on the geomagnetic and solar wind activity.

The paper is organized as follows: In Section 2, we give a brief overview of the Cluster
spacecraft, the RAPID and CIS ions spectrometers and their data products. In Section 3,

118 we explain how we process the data and derive the O^+/H^+ ratio. Section 4 presents the
119 observations and shows how the O^+ and H^+ abundance varies with different parameters
120 controlling the dynamical state of the magnetosphere such as solar wind conditions and
121 also geomagnetic disturbance level. Section 5 discusses the results and related physical
122 processes. Section 6 summarizes the observations.

2. Data and instrumentation

123 The results presented in this study are primarily based on in-situ measurements from
124 the Cluster quartet of spacecraft. The Cluster mission comprises four identical spacecraft
125 flying in a tetrahedron-like formation. More information about the Cluster mission and
126 instrumentation is given in *Escoubet et al.* [1997]. In this paper we have used data from
127 the SC4 spacecraft, since this gives the best data return for our purpose.

128 For the period covered by this study Cluster was in a nearly 90° inclination elliptical
129 orbit with apogee around $19.6 R_E$ and perigee around $4 R_E$. Due to spacecraft orbits in
130 the near-Earth region our observations mainly cover the dawn and dusk flanks and the
131 dayside plasmasheet, mainly the north part, see Figure 1. This Figure shows maps of the
132 energetic O^+ observations, projected into XY_{GSE} , YZ_{GSE} dayside and YZ_{GSE} nightside
133 planes, respectively. This coverage allows us to study the transport of ions from the tail
134 region around the Earth.

135 In addition to the in-situ Cluster observations, we also use solar wind magnetic field and
136 plasma data and geomagnetic disturbance indices to check dependencies and correlations.

137 In this study, we use the AE and Dst indices and not the Kp index as e.g. *Nosé et al.*
138 [2009] or *Mouikis et al.* [2010] because they are more precise (the Kp index has a 3 hours
139 cadence, while the AE and Dst indices have higher time resolution) and have a more direct

140 physical meaning. The Dst index primarily reflects slow (hours) magnetic perturbations
141 caused mainly by ring current enhancements, whereas the AE index reflects short time
142 (minutes) perturbations at high latitudes caused by variations in field-aligned current due
143 to plasma sheet processes such as bursty bulk flow activity.

2.1. Cluster particle measurements

144 We use ion measurements from two different sensors onboard Cluster. Energies above
145 30 keV are covered by RAPID: the Research with Adaptive Particle Imaging Detector
146 [see *Wilken et al.*, 2001], whereas the lower part of the energy range (energies below 40
147 keV) is covered by CIS: the Cluster Ion Spectroscopy instrument [see *Rème et al.*, 2001].

2.1.1. Energetic ion fluxes from RAPID

149 The RAPID Imaging Ion Mass Spectrometer (IIMS) consists of three identical detector
150 heads and use a combination of time-of-flight and energy measurements to classify and
151 bin the incident particles. The three sensors cover 180° in polar angle, and by utilizing the
152 spacecraft spin, RAPID/IIMS provides the distribution of ions with complete coverage
153 of the unit sphere in phase space. Due to a degradation of the central heads on the ion
154 sensor on all spacecraft during the early phase of the mission, only a limited part of the
155 full 3D distribution is available during later stages, however. Since our purpose is to
156 investigate the statistical abundance of two distinct ion species in a particular plasma
157 region, we are not dependent on any 3D abilities, but integrate over all directions to
158 get an omnidirectional flux. Except for extremely anisotropic distributions, the lack of
159 sensitivity in the central sensor does not play any major role [*Kronberg et al.*, 2010].

160 RAPID/IIMS allows for discrimination of various ion species by utilizing time-of-flight
161 and energy information of each incident particle. The resolution of the instrument makes

162 it possible to group ions into three categories; protons (H^+ atomic mass unit 1), helium
163 (He, atomic mass units 2-4) and a common group of heavy ions (atomic mass units 14-
164 16). This latter group is dominated by oxygen, but the mass resolution does not allow
165 for distinction between oxygen, carbon and nitrogen. This group is therefore commonly
166 referred to as the CNO group. The energy ranges are 28 keV – 4 MeV for protons, 137
167 keV – 3.8 MeV for helium and 274 keV – 4 MeV for the CNO group. No information
168 about charge state is possible. For simplicity, we will simply refer to the ratio O^+/H^+ in
169 case of RAPID data, although, we mean the CNO mass group and hydrogen, respectively.

170 The time resolution of the RAPID omnidirectional data is 1 spin (~ 4 seconds), but
171 since the count rates are often very low, we have used 1 minute averages in this study.

172 **2.1.2. Moments and particle measurements from CIS**

173 CIS consists of two sensors. In this paper we use data from the COmposition and
174 DIstribution Function (CODIF) instrument to calculate an omnidirectional flux as done
175 for RAPID. The energy range for CIS is 0.03-40 keV per charge. In addition to the
176 omnidirectional proton and O^+ fluxes, we also utilize plasma moments from the CODIF
177 sensor.

178 As for RAPID we use 1 minute averages and put them on the same timeline as the rest
179 of the data set. Plasma moments are used to identify the plasma region and to filter the
180 data. The CIS instrument has several sensitivity modes, automatically switched in-flight
181 in order to achieve optimal sensitivity and resolution for a particular plasma region. To
182 avoid errors introduced by mode shifting and non-optimal modes we only use data from
183 the so-called magnetospheric mode 13 [see details in *Rème et al., 2001; Dandouras et al.,*
184 *2006*].

185 O^+ measurements by CIS can be slightly contaminated by protons (the major species).
 186 The contamination of H^+ into O^+ is about 0.1-0.3% (depending on energy and on a
 187 particular mode) for low count rates (e.g. in the magnetosphere) for ~ 10 keV ions.
 188 In order to compensate for this contamination of oxygen by protons during active time
 189 periods, we calculate the oxygen intensities as follows: $j^{O^+} = j_m^{O^+} - j^{H^+} \cdot 0.001$, where
 190 $j_m^{O^+}$ and j^{H^+} are the measured oxygen and proton intensities, respectively.

3. Methodology

3.1. Calculation of the O^+/H^+ ratio

191 Our purpose is to compare O^+/H^+ , namely, the ratio between intensities which are
 192 proportional to the number fluxes of O^+ and H^+ [$1/\text{cm}^2 \text{ sr s keV}$] in two energy ranges.
 193 This ratio is equal to the ratio between integral fluxes if the energy range is identical for
 194 the two species. To be able to identify any spectral changes, we use two different energy
 195 ranges, ~ 10 keV (8.1 to 10.3 keV) and the energy band 274–955 keV. These energy bands
 196 are somewhat arbitrarily chosen, and are a compromise between the energy binning of the
 197 two instruments and sufficient statistics. We take a wide energy band for the energetic
 198 ions since the measurements of ions at these energies have relatively low count rates and
 199 wide energy channel divisions. As we do not consider details of any particular acceleration
 200 process but only the response of the particle population to the different geomagnetic and
 201 solar wind activity, the use of the wide energy range of the energetic ions is justified in
 202 this study.

203 For the CIS instrument, the ratio between the number fluxes of O^+ and H^+ is based on
 204 the same energy range; since the energy channels are similar for protons and oxygen. For
 205 RAPID, however, the energy binning for O^+ and H^+ have different thresholds, see energy

206 ranges listed in Table 1. The details on how the RAPID energy channels were rebinned for
 207 the most effective intensities comparison are described in the Appendix. These RAPID
 208 intensities (J^{H^+} and J^{O^+}) are used in the current study.

3.2. Construction of plots

209 Figures 2 to 6 show median intensities for protons and oxygens in two different en-
 210 ergy bands versus the respective geomagnetic or solar wind parameter. The plots are
 211 constructed from data accumulated in the plasma sheet region, defined by plasma beta
 212 value in the range 0.1–10 [Baumjohann et al., 1989]. We have excluded observations
 213 where the magnetic field component B_z was negative in order to avoid the cusp re-
 214 gion. Furthermore, we limit our study to the near-Earth magnetosphere, i.e. distances
 215 $-10 R_E < X_{GSE} < 10 R_E$. We also exclude data from radial distances $< 6 R_E$, as the
 216 sensors can be affected by pileup effects from both penetrating particles (e.g. during solar
 217 proton events) and high count rates.

218 To minimize the effect of skewed distribution, we use median rather than mean values
 219 of the distribution functions. For the same reason, statistical spreads are given as median
 220 absolute deviations (MAD), [see e.g., Venables and Ripley, 1999]. Median value and MAD
 221 are less sensitive to non-normal distribution functions than the mean value and standard
 222 deviation. In order to determine whether differences between values are significant, con-
 223 fidence interval (CI) error bars are given in Figures 2 to 6: $CI = SE \cdot t_{n-1}$, where t_{n-1} is
 224 the t -distribution with n degrees of freedom, $SE = \sigma/\sqrt{n}$ is standard error, where σ , the
 225 standard deviation, was calculated in this case as: $\sigma = 1.4826 \cdot MAD$ [Huber, 1981].

226 The O^+/H^+ ratio is defined as the ratio between median values of the O^+ and H^+
 227 intensities. Correspondingly, errors for the O^+/H^+ ratio are calculated as: $CI_{O^+/H^+} =$

228 $\sqrt{(CI_{O^+}/O^+)^2 + (CI_{H^+}/H^+)^2} \cdot O^+/H^+$. Each value shown in the Figures contains at least
 229 100 measurements.

230 The histogram ranges for Dst, AE, solar wind density and solar wind pressure are de-
 231 fined as follows. The distributions of these parameters are skewed. In order to avoid
 232 outliers, which would take attention away from the more typical values we (1) compute
 233 quartiles of the distribution; (2) define interquartile range (IQR) between first quartile,
 234 Q1, and third quartile, IQR=Q3-Q1; (3) use the 1.5·IQR rule for outliers, which approxi-
 235 mately corresponds to 3σ . This will lead to the histogram ranges between Q1-1.5·IQR and
 236 Q3+1.5·IQR. The behavior of the oxygen and proton intensities are rather complicated
 237 at values which are larger than $\pm 3\sigma$. As an exception we extended the range for the Dst
 238 from -70 nT to -100 nT, in order to cover the whole range for moderated storms.

4. Results

239 Below, we present and discuss how the O^+ , H^+ intensities and O^+/H^+ ratio depend on
 240 respective parameters of the solar-terrestrial coupling in more detail.

4.1. Response to magnetic activity

4.1.1. Geomagnetic storms

242 The interaction between a solar wind shock wave and/or an interplanetary magnetic
 243 cloud with the terrestrial magnetic field can lead to the phenomena called magnetic storms
 244 during which the horizontal component of the Earth's magnetic field decreases dramati-
 245 cally. This decrease is reflected by the Dst index.

246 The response of the ion intensities to the changes in the Dst index is shown in Figure
 247 2 and summarized in Table 2. The intensity of protons at ~ 10 keV and at >274 keV

248 increases approximately in the same manner with decrease of Dst index down to -100
 249 nT (the maximum intensity is ~ 2 times higher than the minimum intensity). Oxygen
 250 intensities at both energies show more dramatic changes with Dst index. Intensities are
 251 up to 30 times higher between the minimum to the maximum. However, during weak
 252 (Dst below -30 nT) and moderate (Dst below -50 nT) magnetic storms, the ratio O^+/H^+
 253 is affected more strongly at ~ 10 keV. Since the ~ 10 keV O^+ intensity grows significantly
 254 (5 times) at Dst from -30 to -100 nT, compared to no change of O^+/H^+ ratio at >274
 255 keV. At the higher energies, the intensities of both species grow together during weak
 256 and moderate storms, therefore, the O^+/H^+ ratio does not clearly change. This agrees
 257 with *Ono et al.* [2009] who found that during dipolarization associated with substorms the
 258 energy density of energetic oxygen does not always increase. However, we see a significant
 259 growth of the >274 keV oxygen, and of O^+/H^+ ratio during the growth phase, from 15
 260 to -30 nT. Therefore, a significant amount of >274 keV oxygen is effectively accelerated
 261 during a storm growth phase.

262 At positive Dst >15 nT the intensity of >274 keV protons is clearly higher compared to
 263 that at Dst $\simeq 0$. This is expected as positive Dst values are associated with a compression
 264 of the magnetopause which can lead to a drift shell displacement. An enhanced intensity
 265 of ~ 10 keV H^+ is observed for positive values of Dst. The effect is not observed in the
 266 O^+ intensity, though.

Based on the observations, we can define linear functional dependence between the
 O^+/H^+ ratio and disturbance level (from -60 to 30 nT):

$$O^+/H^+ = -9.7 \cdot 10^{-4} \times \text{Dst}[\text{nT}] + 3.5 \cdot 10^{-2}.$$

267 The dependency is constructed using a linear least squares fit.

268 We find a weak correlation between proton intensity (both at ~ 10 keV and > 274 keV)
 269 and Dst. This is consistent with results reported by e.g. *Nosé et al.* [2009]; *Mouikis et al.*
 270 [2010]. Also consistent with our results, *Mouikis et al.* [2010] found significantly stronger
 271 correlation of oxygen intensities and geomagnetic activity in the magnetotail region.

272 4.1.2. Response to magnetotail processes

273 Processes in the magnetotail due to e.g. magnetospheric substorms and bursty bulk
 274 flows causing enhanced field-aligned currents leading to auroral electrojet activity reflected
 275 in the AE index.

Figure 3 shows the response in H^+ and O^+ intensities to these processes. The increase in the AE index is associated with an exponential growth by a factor 4 (from the minimum to the maximum) of the ~ 10 keV oxygen intensities. The ~ 10 keV protons only show a slight increase with AE index, (maximum value ~ 1.5 time higher than the lowest value). As above, we can now establish an empirical functional relation between O^+/H^+ ratio and AE index for ~ 10 keV ions

$$O^+/H^+ = 8 \cdot 10^{-5} \times AE[nT] + 3.5 \cdot 10^{-2}.$$

276 The increase of the O^+/H^+ ratio at ~ 10 keV energies means that the oxygen is accelerated
 277 up to these energies more effectively than protons, although sources of their acceleration
 278 have to be different. The study by *Ono et al.* [2009] shows similar results: acceleration
 279 of O^+ at energies of 9 to 36 keV/e during substorms (by electric fields induced by mag-
 280 netic field fluctuations whose frequencies are close to the gyrofrequencies of ions) is more
 281 effective than of H^+ . Event studies by *Zong et al.* [2008, 2009] have shown that bursty
 282 bulk flows can be responsible for supply of the ionospheric oxygen into the near-Earth
 283 magnetosphere.

284 Proton intensities at >274 keV show an exponential increase with AE. Intensities are
285 ~ 8 times higher for high AE values. A similar dependence between AE and >274 keV
286 oxygen intensities are also observed, although the slope has a break at 150-250 nT (strong
287 growth before and moderate after). The highest intensities of >274 keV oxygen, at high
288 AE values are about 33 times higher than the lowest intensities.

289 The effect of substorms on the abundance of the O^+ ions relative to protons is larger
290 at ~ 10 keV, since the O^+ intensity increases more strongly than H^+ . At higher energies,
291 the intensities of the two species seem to increase approximately in the same way starting
292 from $AE \simeq 200$ nT. This again agrees with results obtained by *Ono et al.* [2009] who did
293 not find a clear correlation between substorm-associated dipolarizations and effective O^+
294 acceleration for ions in the energy range 56-212 keV/e. However, our results show a
295 significant increase in intensities of >274 keV oxygen from quiet ($AE \simeq 0-100$ nT) to more
296 disturbed times ($AE \simeq 150-250$ nT). Therefore, a significant amount of >274 keV oxygen
297 is effectively accelerated during weak/moderate substorms or during a substorm growth
298 phase.

4.2. Response to solar wind conditions

299 4.2.1. Response to IMF direction

300 The response of the ion intensities to the changes in IMF direction is shown in Figure
301 4. The IMF direction is represented by the clock angle (CA) defined as the angle between
302 Z_{GSE} and the projection of IMF into the YZ_{GSE} plane.

303 When IMF B_z is negative (i.e. southward IMF), the coupling to the Earth's geomagnetic
304 field is strongest. Southward interplanetary magnetic conditions are typically associated
305 with geomagnetic storm activity.

306 In order to take into account that the changes in particle population do not immediately
307 respond to changes in IMF direction, we only use those measurements during periods
308 where IMF was reasonably stable for at least 30 minutes.

309 The intensity of ~ 10 keV protons increases slightly at the IMF clock angle, -115° in
310 ~ 1.5 times from the minimum to the maximum. For the oxygen intensities the increases
311 are observed at -115° and 125° , in ~ 2.5 times from the minimum to the maximum.

312 High energy particles (energy > 274 keV) are much more sensitive to IMF clock angle
313 variations, especially oxygen ions. The oxygen and proton intensities at > 274 keV are
314 a factor of 10 and 3 higher for southward IMF, respectively. We find a strong positive
315 correlation between the intensities of > 274 keV O^+ , H^+ , the O^+/H^+ ratio and the IMF
316 direction. The energetic ion intensities seem to be correlated with the “openness” of the
317 magnetosphere or change of the clock angle towards the southward direction. However,
318 during the most southward IMF (and dawnward) the acceleration ceases to be effective,
319 the O^+/H^+ ratio does not show significant changes.

320 Since RAPID does not discriminate between charge states, oxygen of solar wind origin
321 (with higher charge states) might explain the strong correlation with IMF clock angle.
322 To check this, we compared our intensities with corresponding intensities of high charge
323 state oxygen, with clear solar wind origin, measured by *Kremser et al.* [1987] in the inner
324 magnetosphere using the AMPTE/CHEM data set. Their results indicate that intensities
325 of high charge state oxygen were about one order of magnitude lower than our RAPID
326 results. Hence, we think that our observations are primarily of ionospheric origin. The
327 effect of IMF orientation is significantly larger for the intensity ratio of the O^+ ions to
328 protons at > 274 keV than at ~ 10 keV. These all suggest a connection between the energy

input to the magnetosphere related to the change of clock angle and the energization of O^+ to high energies (>274 keV).

4.2.2. Solar wind density and pressure

The response of the ion intensities to changes in solar wind density and pressure is shown in Figures 5 and 6, respectively. Intensities of ~ 10 keV oxygen and protons are almost exponentially increasing with solar wind density, (by a factor of ~ 4 for H^+ and a factor of ~ 3 for O^+). For energies >274 keV, we do not see any clear dependence on the solar wind density.

The ~ 10 keV protons and oxygen show almost exponential increase (by a factor ~ 4) with the solar wind dynamic pressure. The proton intensities at >274 keV increase (by a factor of ~ 5) with the solar wind pressure. There is no clear general dependency of the >274 keV oxygen intensities on the solar wind pressure. However, for >274 keV O^+ , we observe a ~ 40 fold increase between ~ 0.5 nPa to 1.75 nPa. At these solar wind pressure values, the energetic oxygen is accelerated more effectively than energetic protons. This is also supported by the fact that in ~ 10 keV oxygen such a tendency is not observed. From ~ 1.75 nPa to 3nPa the intensity of the >274 keV oxygen and protons becomes almost equal.

Statistically, the solar wind density strongly correlates with the plasma sheet density [Borovsky *et al.*, 1998]. This is seen for the ~ 10 keV protons. For ~ 10 keV protons we find a strong correlation between intensity and the solar wind density and pressure.

The increase of ~ 10 keV O^+ intensities is well correlated with the increase of the solar wind dynamic pressure. This is in agreement with earlier studies, e.g. by Cully *et al.* [2003a]; Nosé *et al.* [2003] who found that the ionospheric outflow is strongly affected by

352 the solar wind dynamic pressure. Also in a study by *Echer et al.* [2008], it was shown that
353 a shock compression can lead to enhanced inflow of the oxygen ions into the near-Earth
354 magnetosphere. However, this can be also compression effects, see Section 5.5.

355 Intensities of ~ 10 keV oxygen ions show clear dependencies on solar wind dynamic
356 pressure, as this energy is closer to source energies. This is not the same for energetic ions
357 which are not closely related with outflow energies and require stronger acceleration. The
358 observed prominent increase in the oxygen intensities for solar wind dynamic pressure up
359 to 1.5 nPa is more likely related to acceleration mechanisms due to the thinning of the
360 plasma sheet, see Section 5.4. The largest increase in the energetic particle intensities is
361 seen during the transition period between quiet and disturbed times.

5. Discussion

5.1. Comparison to other observations

362 Our energy density results listed in Table 3 (see calculations in Appendix, Equation)
363 are comparable to the observations in the near-Earth plasma sheet made by e.g. *Gloeckler*
364 *et al.* [1985], *Hamilton et al.* [1988] and *Nosé et al.* [2001]. We do not observe the dramatic
365 differences between quiet and disturbed times reported in these earlier studies, though. A
366 possible reason is that we have used median values rather than mean values, and thus avoid
367 effects of outliers and strongly scattered distributions. Also, the definitions of quiet and
368 disturbed times, are based on AE index and Dst indices and differs from earlier studies.
369 One could notice that the difference between quiet and disturbed times for the ~ 10 keV
370 ions is stronger when using the Dst index as definition. Taking even more negative values
371 of Dst will lead to the higher O^+/H^+ ratios. Therefore, the dynamics of the ~ 10 keV
372 particles in the near-Earth magnetosphere is more strongly correlated with the Dst index.

5.2. Comparison to ionospheric outflow observations

373 Ion outflow rates (at 0.01-17 keV) can vary by a factor of 30 between quiet and very
374 disturbed periods *Yau et al.* [1985]. Our result shows that the >274 keV oxygen intensity
375 is about 33 times higher during very disturbed periods than during quiet time (here AE
376 index is used). For comparison, the ~ 10 keV O^+ intensity increases a factor 4 between
377 quiet and very disturbed times. Acceleration of ~ 10 keV oxygen seems to be more effective
378 during disturbed times, while for >274 keV oxygen acceleration primary occurs during
379 transitions from quiet to disturbed periods. Such slope break between quiet and disturbed
380 states is not observed in the ionospheric O^+ outflow [*Yau et al.*, 1985; *Cully et al.*, 2003a].

381 For protons, the intensities of ~ 10 keV ions are only slightly different during disturbed
382 periods than during quiet times. The intensity of protons with energies >274 keV increases
383 by a factor of about 8 between quiet and disturbed times. For comparison, for auroral
384 and polar protons outflow an increase of the order of 5 was reported by *Yau et al.* [1985].

385 The ratio between quiet and disturbed times for the ion ionospheric outflow is higher
386 than those observed in the near-Earth magnetosphere at ~ 10 keV but similar to those
387 observed at >274 keV. These appears to be a connection between the energetic ion inten-
388 sities and ion outflow that changes with geomagnetic activity. The fact that the ratios
389 between quiet and disturbed times are higher for the more energetic and heavier particles
390 means that the ions are more effectively accelerated up to these energies. This is consis-
391 tent with explanation by *Moebius et al.* [1987] and many other studies thereafter, that
392 the acceleration process in the near-Earth magnetosphere is mass dependent, as it is more
393 effective for the heavier particles.

5.3. Response of protons to geomagnetic activity and solar wind conditions

394 As shown in Section 4.2.1, the intensity of ~ 10 keV protons does not seem to be directly
395 affected by dayside reconnection. Response to IMF direction would be expected, though,
396 as it is likely to be associated with dayside reconnection and then consequent transfer of
397 the solar wind ions into the magnetosphere and subsequent acceleration. By the same
398 token, magnetic storms and substorm activity are typically also related to the dayside
399 reconnection. In addition storms and substorms are typically associated with enhanced
400 outflow. As a consequence, more ions would be energized in the magnetosphere. Still, the
401 correlation between the ~ 10 keV proton intensities on one hand, and geomagnetic activity,
402 solar wind dynamic pressure and clock angle on the other hand is less pronounced than
403 for the ~ 10 keV oxygen, see Sections 4.1.1, 4.1.2 and 4.2.1.

404 These observations can be explained as follows. Heavier ions (O^+) require additional
405 forces such as electric fields, wave activity or stronger gradients in pressure and tempera-
406 ture to escape from the ionosphere. These processes are primarily driven by enhanced day-
407 side reconnection and the subsequent processes reflected by increased disturbance levels.
408 Protons, on the other hand, with their much lower escape energies, are not so dependent
409 on these external forces. Solar illumination alone suffices to extract a significant number
410 of light ions from the ionosphere. Therefore, the strong dependence on the disturbance
411 parameters of the ~ 10 keV protons is not observed.

5.4. Changes during growth phase

412 Why would we expect an increase in energetic oxygen intensities during the transition
413 period between quiet and disturbed times (substorm growth phase)? The increased solar
414 wind pressure (or loading of the energy during Dungey cycle) can lead to the plasma sheet

415 thinning [e.g., *Sauvaud et al.*, 1996] and therefore to a more effective acceleration of the
 416 heavy ions [e.g., *Ganguli et al.*, 1995]. There are different regimes of particle motion in the
 417 plasma sheet derived by *Büchner and Zeleny* [1986]. According to their work the particles
 418 are accelerated most effectively when parameter $\kappa = \sqrt{\frac{r_{curv}}{r_g}} \sim 1$, where r_{curv} is the radius
 419 of magnetic field curvature and r_g is ion gyroradius. Under these conditions the particle
 420 trajectories become stochastic and particles are effectively accelerated by quasi-stationary
 421 dawn-dusk electric fields. A decrease in plasma sheet thickness, e.g. in response to an
 422 increase of the lobe magnetic field, will lead to larger region where stochastic acceleration
 423 of energetic ions can take place, as it will decrease the parameter κ which is quite large
 424 in the plasma sheet for solar wind protons [*Ashour-Abdalla et al.*, 2009].

5.5. Changes with solar wind pressure

425 Increased solar wind dynamic pressure leads to a compression of the magnetosphere and
 426 the same total quantity of particles have to be distributed over a smaller volume. Con-
 427 sequently, the particle density/intensity will be higher and this will lead to the observed
 428 correlation. The observed differences in behavior between ~ 10 keV (where a correlation
 429 is evident) and > 274 keV ions (no clear correlation with dynamic solar wind pressure)
 430 can be explained as follows: the plasma sheet may become thinner as result of very strong
 431 solar wind pressure, and therefore, the gyroradius versus curvature radius effect discussed
 432 above may be relevant also here.

433 On other hand, the correlation with the solar wind dynamic pressure can be related to
 434 the Earth's ionosphere which may provide heavier ions to the magnetotail during enhanced
 435 solar wind dynamic pressure, see *Cully et al.* [2003a]; *Nosé et al.* [2003]; *Echer et al.* [2008].

6. Summary

436 Based on seven years of ion composition data from Cluster observations at radial dis-
437 tances $-10 R_E < X_{GSE} < 10 R_E$, we find the following:

438 (1) H^+ intensities at ~ 10 keV show only a slight correlation with geomagnetic conditions
439 (Dst and AE indices) and interplanetary magnetic field orientation. Solar wind dynamic
440 pressure and density (i.e. effects of magnetospheric compression) seem to have a larger
441 effect on the ~ 10 keV H^+ intensities.

442 (2) O^+ ion intensities at ~ 10 keV are more affected by geomagnetic storms and sub-
443 storms than >274 keV O^+ ion intensities, than their corresponding hydrogen counterparts.
444 The >274 keV O^+ energization/acceleration seem to be strongest during the transition
445 period from quiet to disturbed times, i.e., during growth phases rather than during the
446 disturbed phases itself. The ~ 10 keV ions do not reveal such a dependence.

447 (3) We find a strong positive correlation between the flux of >274 keV O^+ , H^+ , the
448 O^+/H^+ ratio and the IMF direction. This demonstrates a connection between energy
449 input to the magnetosphere and effective energization of energetic ions.

450 (4) The intensity ratio between quiet and disturbed times for the ionospheric ion outflow
451 is similar to those observed in the near-Earth magnetosphere at >274 keV. Therefore, the
452 observed increase of the energetic ion intensity during disturbed time is not only due to
453 a more effective acceleration but also due to enhanced ion outflow.

454 (5) Our results seem to confirm the conclusion of *Moebius et al.* [1987] and many other
455 studies afterwards, in that acceleration processes in the near-Earth magnetosphere are
456 mass dependent, because it is more effective for the heavier ions (O^+/H^+ ratio higher).

Appendix A: Construction of RAPID O⁺/H⁺ ratio

We shall refer to the corresponding differential particle fluxes, j_i , from the eight energy channels, $(E_n^{H^+}, E_n^{O^+})$, of the RAPID instrument as $j_1^{H^+}$ to $j_8^{H^+}$ and $j_1^{O^+}$ to $j_8^{O^+}$, respectively (see Table 1).

The lowest energy channel for oxygen, $E_1^{O^+}$ (with energy range 84–274 keV), is contaminated by protons, and cannot be used [Daly and Kronberg, 2010]. The count rates in energy channels above 1 MeV (i.e., E_6 , E_7 and E_8) are usually extremely low for both species. Useful O⁺ channels are therefore energy channels $E_2^{O^+} - E_5^{O^+}$, covering energies from 274 to ~955 keV. For protons, corresponding to this energy range, parts of $E_4^{H^+}$ and $E_5^{H^+}$ have to be used. We have decided to use both these H⁺ channels rather than only one $E_5^{H^+}$ and the part of the $E_2^{O^+}$, respectively, for better statistics. To construct O⁺ and H⁺ energy bins with matching energies, we proceed as follows:

1. Determine the integrated oxygen intensity, J^{O^+} , at energies from 274 up to ~955 keV. The integrated intensity is determined as the differential fluxes, $j_i^{O^+}$ multiplied by respective $\Delta E_i^{O^+}$:

$$J^{O^+} = (j_2^{O^+} \cdot \Delta E_2^{O^+} + j_3^{O^+} \cdot \Delta E_3^{O^+} + j_4^{O^+} \cdot \Delta E_4^{O^+} + j_5^{O^+} \cdot \Delta E_5^{O^+}) [1/(cm^3 \cdot sr \cdot s)];$$

2. Obtain spectral index γ , in order to cut the part of the $E_4^{H^+}$, see Figure 7 for illustration. For this we use fluxes from two adjacent energy channels ($E_4^{H^+}$ and $E_5^{H^+}$) and their effective energies, E_{eff} , the energy at which the spectrum, $A \cdot E_{eff}^{-\gamma}$, with given A and γ has the differential flux equal $J/\Delta E$:

$$\gamma = \ln(j_5^{H^+} / j_4^{H^+}) / \ln(E_{eff4}^{H^+} / E_{eff5}^{H^+}),$$

468 where E_{eff} in this case is calculated as the geometric mean energy of the respective
 469 energy channels. See more details on these calculations in the RAPID Calibration Report
 470 [*Kronberg and Daly, 2009*], chapter B.1;

3. Determine $j_x^{H^+}$ — i.e., the H^+ differential flux at the virtual energy $E_x^{H^+}$, 274-374
 keV (which matches the O^+ energy channel), with effective energy $E_{effx}^{H^+} = \sqrt{274 \cdot 374}$
 keV and determined γ , see Figure 7:

$$j_x^{H^+} = j_4^{H^+} \cdot e^{-\gamma \cdot \ln(E_{effx}^{H^+}/E_{eff4}^{H^+})};$$

471 4. Determine integrated proton intensity, J^{H^+} , at energies from 274 up to 962 keV:
 472 $J^{H^+} = j_x^{H^+} \cdot \Delta E_x^{H^+} + j_5^{H^+} \cdot \Delta E_5^{H^+}$. With this procedure, we establish a virtual proton
 473 energy channel with the same lower energy threshold as for the oxygen. The slightly
 474 different upper energy level (962 and 948 keV, respectively) does not play any role here;

475 5. Define the intensity ratio: $\frac{O^+}{H^+} = \frac{J^{O^+}}{J^{H^+}}$

In order to compare our results with other observations we need to use the energy
 density ratio. To establish the energy density ratio, we assume that the relative geometric
 factors are correct for both species:

$$\frac{O^+}{H^+} = \frac{\pi \sqrt{2m_O} \cdot \sqrt{E_{eff}} \cdot J^{O^+} \Delta E}{\pi \sqrt{2m_H} \cdot \sqrt{E_{eff}} \cdot J^{H^+} \Delta E} = \frac{4 \cdot J^{O^+}}{J^{H^+}}, \quad (A1)$$

476 where $O^+ = \sqrt{m_O} \cdot \sqrt{E_{eff}} \cdot J^{O^+}$ and $H^+ = \sqrt{m_H} \cdot \sqrt{E_{eff}} \cdot J^{H^+}$.

477 This calculation is based on the assumption that the effective energy is equal to the
 478 geometric mean of the corresponding energy thresholds. However, in our case the width of
 479 the energetic channel is quite large and this will lead to the deviation of the energy density
 480 from the value calculated using the effective energy as the geometric mean. The way to
 481 calculate this deviation one can find in the the RAPID Calibration Report [*Kronberg and*

482 *Daly, 2009*], chapter B.3. The deviation is estimated to be $\sim 65\%$ and error bar $\pm 30\%$
483 from the value of the energy density calculated in Equation A1. For these calculations
484 the typical range of γ values derived from our data base were taken: for O^+ $\gamma = 2-3.5$ and
485 for H^+ $\gamma = 3.5-6.5$. The statistical errors of the energy density and the error due to the
486 large width of the energy channels are added in this case.

487 **Acknowledgments.** We thank the Deutsches Zentrum für Luft und Raumfahrt (DLR)
488 for supporting the RAPID instrument at MPS under grant 50 OC 1101. The authors are
489 grateful for the use of the OMNI data base providing AE, Dst and solar wind parameters.
490 E. Grigorenko thanks grants RFBR Nr. 10-02-00135; 10-02-93114; 12-02-92614 and grant
491 of Leading Scientific Schools HIII-623.2012.2.

References

- 492 Ashour-Abdalla, M., J.-M. Bosqued, M. El-Alaoui, V. Perroomian, M. Zhou, R. Richard,
493 R. Walker, A. Runov, and V. Angelopoulos (2009), A simulation study of particle
494 energization observed by THEMIS spacecraft during a substorm, *J. Geophys. Res.*,
495 *114*, A09204, doi:10.1029/2009JA014126.
- 496 Baumjohann, W., G. Paschmann, and C. A. Cattell (1989), Average plasma properties in
497 the central plasma sheet, *J. Geophys. Res.*, *94*, 6597–6606.
- 498 Borovsky, J. E., M. F. Thomsen, and R. C. Elphic (1998), The driving of the plasma
499 sheet by the solar wind, *J. Geophys. Res.*, *103*, 17,617–17,640, doi:10.1029/97JA02986.
- 500 Büchner, J., and L. M. Zeleny (1986), Deterministic chaos in the dynamics of charged
501 particles near a magnetic field reversal, *Physics Letters A*, *118*, 395–399, doi:10.1016/
502 0375-9601(86)90268-9.

503 Chappell, C. R., T. E. Moore, and J. H. Waite, Jr. (1987), The ionosphere as a fully
504 adequate source of plasma for the earth's magnetosphere, *J. Geophys. Res.*, *92*, 5896–
505 5910, doi:10.1029/JA092iA06p05896.

506 Chappell, C. R., B. L. Giles, T. E. Moore, D. C. Delcourt, P. D. Craven, and M. O.
507 Chandler (2000), The adequacy of the ionospheric source in supplying magnetospheric
508 plasma, *Journal of Atmospheric and Solar-Terrestrial Physics*, *62*, 421–436, doi:10.
509 1016/S1364-6826(00)00021-3.

510 Cladis, J. B. (1986), Parallel acceleration and transport of ions from polar ionosphere to
511 plasma sheet, *Geophys. Res. Lett.*, *13*, 893–896, doi:10.1029/GL013i009p00893.

512 Cully, C. M., E. F. Donovan, A. W. Yau, and G. G. Arkos (2003a), Akebono/Suprathermal
513 Mass Spectrometer observations of low-energy ion outflow: Dependence on mag-
514 netic activity and solar wind conditions, *J. Geophys. Res.*, *108*, 1093, doi:10.1029/
515 2001JA009200.

516 Cully, C. M., E. F. Donovan, A. W. Yau, and H. J. Opgenoorth (2003b), Supply of
517 thermal ionospheric ions to the central plasma sheet, *J. Geophys. Res.*, *108*, 1092, doi:
518 10.1029/2002JA009457.

519 Daglis, I. A., and W. I. Axford (1996), Fast ionospheric response to enhanced activity
520 in geospace: Ion feeding of the inner magnetotail, *J. Geophys. Res.*, *101*, 5047–5066,
521 doi:10.1029/95JA02592.

522 Daglis, I. A., Y. Kamide, C. Mouikis, G. D. Reeves, E. T. Sarris, K. Shiokawa,
523 and B. Wilken (2000), “Fine Structure” of the Storm-Substorm Relationship: Ion
524 Injections During Dst Decrease, *Advances in Space Research*, *25*, 2369–2372, doi:
525 10.1016/S0273-1177(99)00525-6.

526 Daly, P. W., and E. A. Kronberg (2010), RAPID Products at the Cluster Active
527 Archive, in *The Cluster Active Archive, Studying the Earth's Space Plasma Envi-*
528 *ronment*, edited by Laakso, H., Taylor, M., & Escoubet, C. P., pp. 145–158, doi:
529 10.1007/978-90-481-3499-1_9.

530 Dandouras, I., A. Barthe, E. Penou, H. Rème, S. McCaffrey, C. Vallat, L. M. Kistler, and
531 The Cis Team (2006), Archival of the Cluster ion spectrometry (CIS) data in the Cluster
532 active archive (CAA), in *Cluster and Double Star Symposium, ESA Special Publication*,
533 vol. 598.

534 Echer, E., A. Korth, Q.-G. Zong, M. Fränz, W. D. Gonzalez, F. L. Guarnieri, S. Y. Fu,
535 and H. Reme (2008), Cluster observations of O⁺ escape in the magnetotail due to shock
536 compression effects during the initial phase of the magnetic storm on 17 August 2001,
537 *J. Geophys. Res.*, *113*, A05209, doi:10.1029/2007JA012624.

538 Escoubet, C. P., R. Schmidt, and M. L. Goldstein (1997), Cluster - Science and Mission
539 Overview, *Space Sci. Rev.*, *79*, 11–32.

540 Fu, S. Y., Q. G. Zong, T. A. Fritz, Z. Y. Pu, and B. Wilken (2002), Composition signatures
541 in ion injections and its dependence on geomagnetic conditions, *J. Geophys. Res.*, *107*,
542 1299, doi:10.1029/2001JA002006.

543 Ganguli, G., P. J. Palmadesso, J. Fedder, and A. T. Y. Lui (1995), Role of Fermi accel-
544 eration in explosive enhancement of cross-tail current in late substorm growth phase,
545 *Geophys. Res. Lett.*, *22*, 2405–2408, doi:10.1029/95GL02488.

546 Glocer, A., G. Tóth, Y. Ma, T. Gombosi, J.-C. Zhang, and L. M. Kistler (2009), Multifluid
547 Block-Adaptive-Tree Solar wind Roe-type Upwind Scheme: Magnetospheric composi-
548 tion and dynamics during geomagnetic storms – Initial results, *J. Geophys. Res.*, *114*,

- 549 A12203, doi:10.1029/2009JA014418.
- 550 Gloeckler, G., F. M. Ipavich, B. Wilken, W. Stuedemann, and D. Hovestadt (1985), First
551 composition measurement of the bulk of the storm-time ring current (1 to 300 keV/e)
552 with AMPTE-CCE, *Geophys. Res. Lett.*, *12*, 325–328, doi:10.1029/GL012i005p00325.
- 553 Hamilton, D. C., G. Gloeckler, F. M. Ipavich, B. Wilken, and W. Stuedemann (1988),
554 Ring current development during the great geomagnetic storm of February 1986, *J.*
555 *Geophys. Res.*, *93*, 14,343–14,355, doi:10.1029/JA093iA12p14343.
- 556 Huber, P. J. (1981), *Robust Statistics*, pp. 107–108, John Wiley & Sons, New York.
- 557 Huddleston, M. M., C. R. Chappell, D. C. Delcourt, T. E. Moore, B. L. Giles, and
558 M. O. Chandler (2005), An examination of the process and magnitude of ionospheric
559 plasma supply to the magnetosphere, *J. Geophys. Res.*, *110*, A12,202, doi:10.1029/
560 2004JA010401.
- 561 Kistler, L. M., E. Möbius, B. Klecker, G. Gloeckler, and F. M. Ipavich (1990), Spatial
562 variations in the suprathermal ion distributions during substorms in the plasma sheet,
563 *J. Geophys. Res.*, *95*, 18,871–18,885, doi:10.1029/JA095iA11p18871.
- 564 Kistler, L. M., D. J. Larson, E. Möbius, and W. Baumjohann (1994), The decay of
565 superthermal ion fluxes during the substorm recovery phase, *J. Geophys. Res.*, *99*,
566 10,941–10,954, doi:10.1029/93JA03180.
- 567 Kistler, L. M., C. G. Mouikis, B. Klecker, and I. Dandouras (2010), Cusp as a source for
568 oxygen in the plasma sheet during geomagnetic storms, *J. Geophys. Res.*, *115*, A03209,
569 doi:10.1029/2009JA014838.
- 570 Kitamura, N., et al. (2010), Observations of very-low-energy (<10 eV) ion outflows
571 dominated by O⁺ ions in the region of enhanced electron density in the polar

572 cap magnetosphere during geomagnetic storms, *J. Geophys. Res.*, *115*, A00J06, doi:
573 10.1029/2010JA015601.

574 Kremser, G., W. Stuedemann, B. Wilken, and G. Gloeckler (1987), Observations of spatial
575 distribution of energetic O^{3+} , O^{4+} , and O^{5+} ions in the magnetosphere, *Geophys. Res.*
576 *Lett.*, *14*, 685–688, doi:10.1029/GL014i007p00685.

577 Kronberg, E. A., and P. W. Daly (2009), Calibration report of the RAPID measurements
578 in the Cluster Active Archive (CAA), *Tech. Rep. CAA-EST-CR-RAP*.

579 Kronberg, E. A., P. W. Daly, I. Dandouras, S. Haaland, and E. Georgescu (2010),
580 Generation and Validation of Ion Energy Spectra Based on Cluster RAPID and CIS
581 Measurements, in *The Cluster Active Archive, Studying the Earth's Space Plasma En-*
582 *vironment*, edited by Laakso, H., Taylor, M., & Escoubet, C. P., pp. 301–306, doi:
583 10.1007/978-90-481-3499-1_20.

584 Lennartsson, W., and E. G. Shelley (1986), Survey of 0.1- to 16-keV/e plasma sheet ion
585 composition, *J. Geophys. Res.*, *91*, 3061–3076, doi:10.1029/JA091iA03p03061.

586 Lockwood, M., J. H. Waite, Jr., T. E. Moore, C. R. Chappell, and J. F. E. Johnson
587 (1985), A new source of suprathermal O^+ ions near the dayside polar cap boundary, *J.*
588 *Geophys. Res.*, *90*, 4099–4116, doi:10.1029/JA090iA05p04099.

589 Moebius, E., M. Scholer, B. Klecker, D. Hovestadt, G. Gloeckler, and F. M. Ipavich
590 (1987), *Acceleration of ions of ionospheric origin in the plasmashet during substorm*
591 *activity*, pp. 231–234, In: *Magnetotail Physics*, edited by A. T. Y. Lui, The Johns
592 Hopkins University Press, Baltimore, Md.

593 Moore, T. E., and J. L. Horwitz (2007), Stellar ablation of planetary atmospheres, *Reviews*
594 *of Geophysics*, *45*, 3002, doi:10.1029/2005RG000194.

- 595 Mouikis, C. G., L. M. Kistler, Y. H. Liu, B. Klecker, A. Korth, and I. Dandouras (2010),
596 The H^+ and O^+ content of the plasma sheet at 15-19 Re as a function of geomagnetic
597 and solar activity, *J. Geophys. Res.*, *115*, A00J16, doi:10.1029/2010JA015978.
- 598 Nilsson, H., E. Engwall, A. Eriksson, P. A. Puhl-Quinn, and S. Arvelius (2010),
599 Centrifugal acceleration in the magnetotail lobes, *Ann. Geophys.*, *28*, 569–576, doi:
600 10.5194/angeo-28-569-2010.
- 601 Nilsson, H., et al. (2008), Transients in oxygen outflow above the polar cap as observed by
602 the Cluster spacecraft, *Ann. Geophys.*, *26*, 3365–3373, doi:10.5194/angeo-26-3365-2008.
- 603 Nosé, M., S. Ohtani, K. Takahashi, A. T. Y. Lui, R. W. McEntire, D. J. Williams, S. P.
604 Christon, and K. Yumoto (2001), Ion composition of the near-Earth plasma sheet in
605 storm and quiet intervals: Geotail/EPIC measurements, *J. Geophys. Res.*, *106*, 8391–
606 8404, doi:10.1029/2000JA000376.
- 607 Nosé, M., R. W. McEntire, and S. P. Christon (2003), Change of the plasma sheet ion
608 composition during magnetic storm development observed by the Geotail spacecraft, *J.*
609 *Geophys. Res.*, *108*, 1201, doi:10.1029/2002JA009660.
- 610 Nosé, M., A. Ieda, and S. P. Christon (2009), Geotail observations of plasma sheet ion
611 composition over 16 years: On variations of average plasma ion mass and O^+ triggering
612 substorm model, *J. Geophys. Res.*, *114*, A07,223, doi:10.1029/2009JA014203.
- 613 Ono, Y., M. Nosé, S. P. Christon, and A. T. Y. Lui (2009), The role of magnetic field
614 fluctuations in nonadiabatic acceleration of ions during dipolarization, *J. Geophys. Res.*,
615 *114*, A05209, doi:10.1029/2008JA013918.
- 616 Rème, H., et al. (2001), First multispacecraft ion measurements in and near the Earth's
617 magnetosphere with the identical Cluster ion spectrometry (CIS) experiment, *Ann.*

618 *Geophys.*, *19*, 1303–1354.

619 Sauvaud, J. A., C. Jacquey, T. Beutier, R. P. Lepping, C. T. Russell, R. J. Belian, and
620 A. T. Y. Lui (1996), Dynamics of the magnetospheric mid-tail induced by substorms; A
621 multisatellite study, *Advances in Space Research*, *18*, 35–43, doi:10.1016/0273-1177(95)
622 00992-2.

623 Sharp, R. D., D. L. Carr, W. K. Peterson, and E. G. Shelley (1981), Ion streams in the
624 magnetotail, *J. Geophys. Res.*, *86*, 4639–4648, doi:10.1029/JA086iA06p04639.

625 Venables, W. N., and B. D. Ripley (1999), *Modern Applied Statistics with S-PLUS*, 3rd
626 edn. ed., Springer.

627 von Steiger, R., T. H. Zurbuchen, and D. J. McComas (2010), Oxygen flux in the
628 solar wind: Ulysses observations, *Geophys. Res. Lett.*, *37*, L22101, doi:10.1029/
629 2010GL045389.

630 Welling, D. T., V. K. Jordanova, S. G. Zaharia, A. Glocer, and G. Toth (2011), The effects
631 of dynamic ionospheric outflow on the ring current, *J. Geophys. Res.*, *116*, A00J19, doi:
632 10.1029/2010JA015642.

633 Wilken, B., et al. (2001), First results from the RAPID imaging energetic particle spec-
634 trometer on board Cluster, *Ann. Geophys.*, *19*, 1355–1366.

635 Yau, A. W., and M. Andre (1997), Sources of Ion Outflow in the High Latitude Ionosphere,
636 *Space Science Reviews*, *80*, 1–25, doi:10.1023/A:1004947203046.

637 Yau, A. W., B. A. Whalen, W. K. Peterson, and E. G. Shelley (1984), Distribution of
638 upflowing ionospheric ions in the high-altitude polar cap and auroral ionosphere, *J.*
639 *Geophys. Res.*, *89*, 5507–5522, doi:10.1029/JA089iA07p05507.

- 640 Yau, A. W., L. Lenchyshyn, E. G. Shelley, and W. K. Peterson (1985), Energetic auroral
641 and polar ion outflow at DE 1 altitudes: Magnitude, composition, magnetic activity
642 dependence, and long-term variations, *J. Geophys. Res.*, *90*, 8417–8432, doi:10.1029/
643 JA090iA09p08417.
- 644 Zong, Q.-G., H. Zhang, S. Y. Fu, Y. F. Wang, Z. Y. Pu, A. Korth, P. W. Daly, and T. A.
645 Fritz (2008), Ionospheric oxygen ions dominant bursty bulk flows: Cluster and Double
646 Star observations, *J. Geophys. Res.*, *113*, A07S23, doi:10.1029/2007JA012764.
- 647 Zong, Q.-G., et al. (2009), Vortex-like plasma flow structures observed by Cluster at the
648 boundary of the outer radiation belt and ring current: A link between the inner and
649 outer magnetosphere, *J. Geophys. Res.*, *114*, A10211, doi:10.1029/2009JA014388.

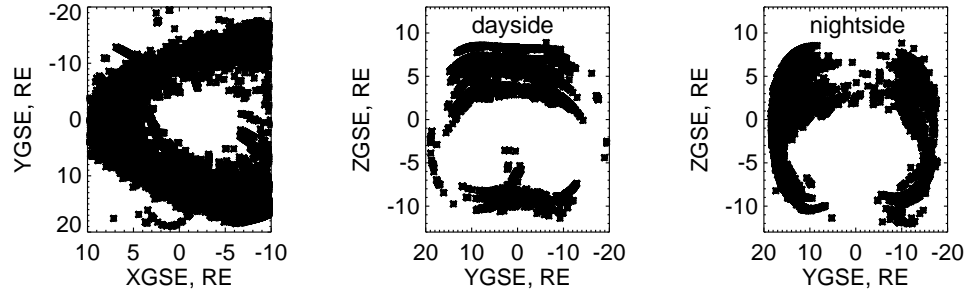


Figure 1. Maps of the location of the energetic oxygen observations, from left in XY_{GSE} , YZ_{GSE} dayside ($X_{GSE} > 0$) and YZ_{GSE} nightside ($X_{GSE} \leq 0$) planes.

Table 1. Lower thresholds of energy channels for protons and oxygen for RAPID. Note that energy channels for H^+ and O^+ are not overlapping. To make the O^+/H^+ ratio meaningful, we therefore fit a spectrum and derive an additional H^+ energy channel for RAPID, see Appendix.

Channel	Energy range H^+ , keV	Energy range O^+ , keV
1	28-64 ^a	84 ^b
2	75	274
3	92	414
4	160	498
5	374	638
6	962	948
7	1885	1414
8	— ^c	2539
Upper	4007	4046

^a Energy gap between hydrogen 1 & 2

^b CNO channel 1 contaminated at times, suppressed

^c 8th channel not accessible for hydrogen

Table 2. Response of ion intensity to changes in the Dst index.

Particles	Compression ^a	Growth phase ^b	Weak-moderate ^c	Quiet-Storm time ^d	Min-Max ^e
	Dst>15 nT ^f	-30<Dst<15 nT	-105<Dst<-30 nT	-105<Dst<0 nT	
H ⁺ ~10 keV	no change	no change	+1.6x ^g	+1.4x	+2x
O ⁺ ~10 keV	-2x ^g	+1.5x	+8x	+14x	+13x
O ⁺ /H ⁺ ~10 keV	-2x	+1.7x	+5x	+10x	+22x
H ⁺ >274 keV	+2x	+1.5x	+1.6x	+2.3x	+2.4x
O ⁺ >274 keV	-8x	+3x	+1.6x	+3.6x	+30x
O ⁺ /H ⁺ >274 keV	-16x	+2x	no change	+1.6x	+30x

^a Difference between ion intensities at ~22.5 nT and ~0 nT (here and further, the mean values of the corresponding bins), namely during magnetospheric compression.

^b Difference between ion intensities at ~0 nT and ~-22.5 nT, namely between beginning and end of the growth phase.

^c Difference between ion intensities at ~-37.5 nT and ~-97.5 nT, namely between weak and moderate storms.

^d Difference between ion intensities at ~0 nT and ~-97.5 nT, namely between quiet and storm time.

^e Difference between minimum and maximum ion intensities in Figure 2.

^f This value and corresponding values in the next columns are the thresholds of the ranges.

^g “-*x” is decrease in * times and “+*x” is increase in * times.

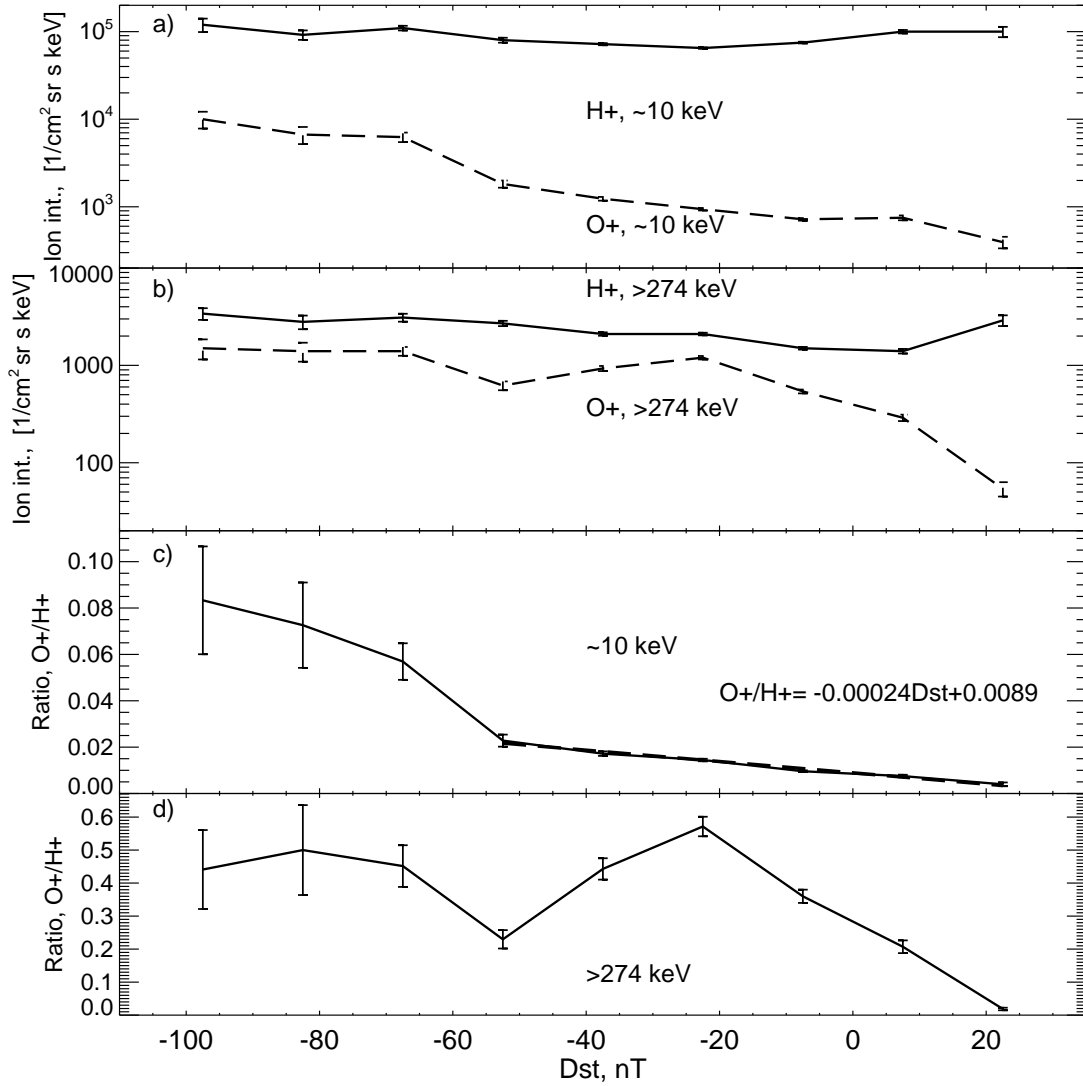


Figure 2. a) Dependencies on Dst index of (a) proton and oxygen intensities at ~ 10 keV, (b) proton and oxygen intensities for >274 keV, (c) ratio O^+/H^+ for intensities at ~ 10 keV and (d) ratio O^+/H^+ for intensities at >274 keV. The dashed line in panel 3 indicates a linear fit to the ratio values. Error bars indicate 99% confidence intervals.

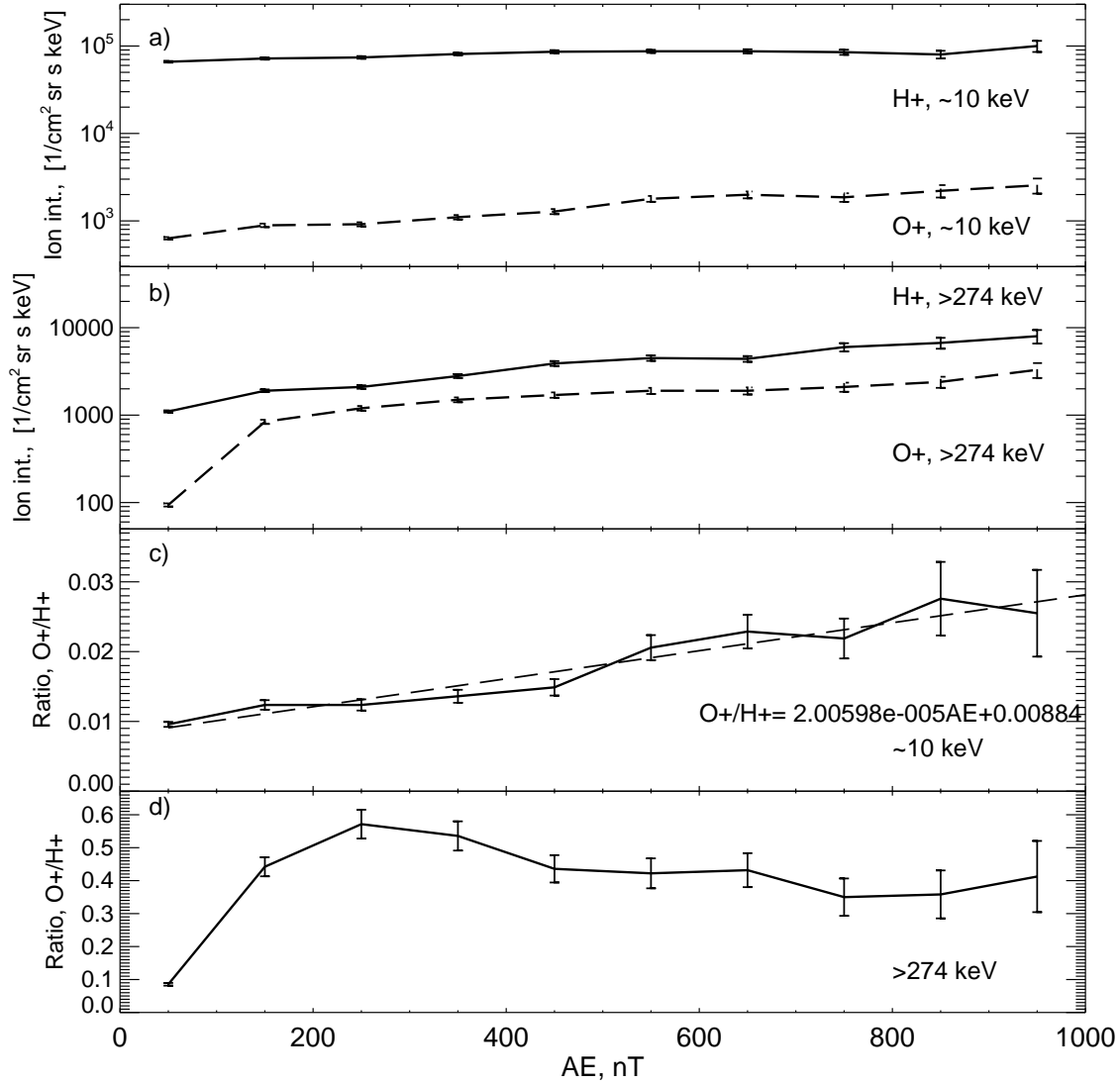


Figure 3. Dependencies on AE index of (a) proton and oxygen intensities at $\sim 10 \text{ keV}$, (b) proton and oxygen intensities at $>274 \text{ keV}$, (c) ratio O^+/H^+ for intensities at $\sim 10 \text{ keV}$ and (d) ratio O^+/H^+ for intensities at $>274 \text{ keV}$. The dashed line in panel 3 indicates a linear fit to the ratio values. Error bars indicate 99% confidence intervals.

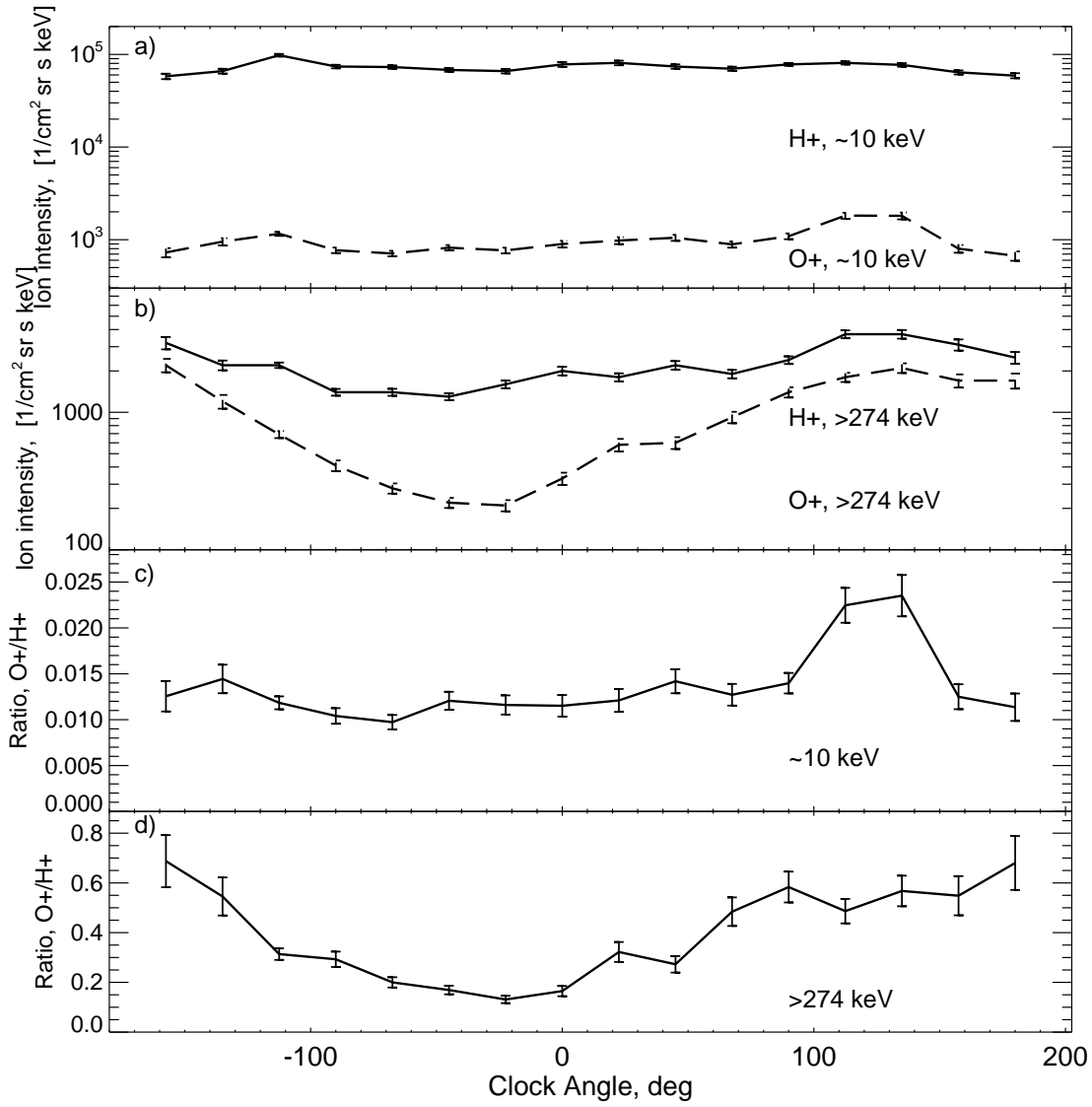


Figure 4. Dependencies on Clock Angle of (a) proton and oxygen intensities at ~ 10 keV, (b) proton and oxygen intensities at >274 keV, (c) ratio O^+/H^+ for intensities at ~ 10 keV and (d) ratio O^+/H^+ for intensities at >274 keV.

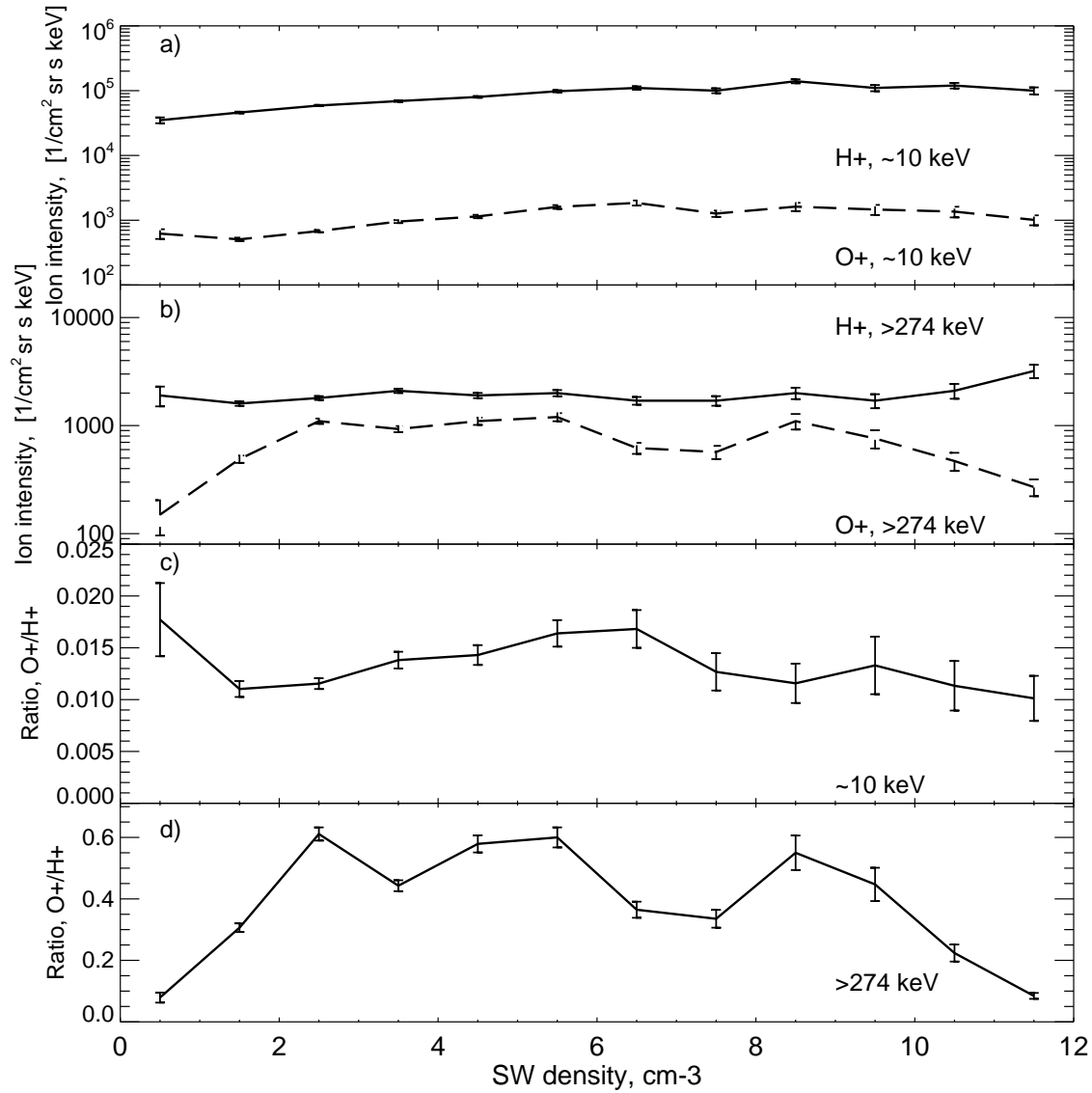


Figure 5. Dependencies on solar wind density of (a) proton and oxygen intensities at ~10 keV, (b) proton and oxygen intensities at >274 keV, (c) ratio O⁺/H⁺ for intensities at ~10 keV and (d) ratio O⁺/H⁺ for intensities at >274 keV.

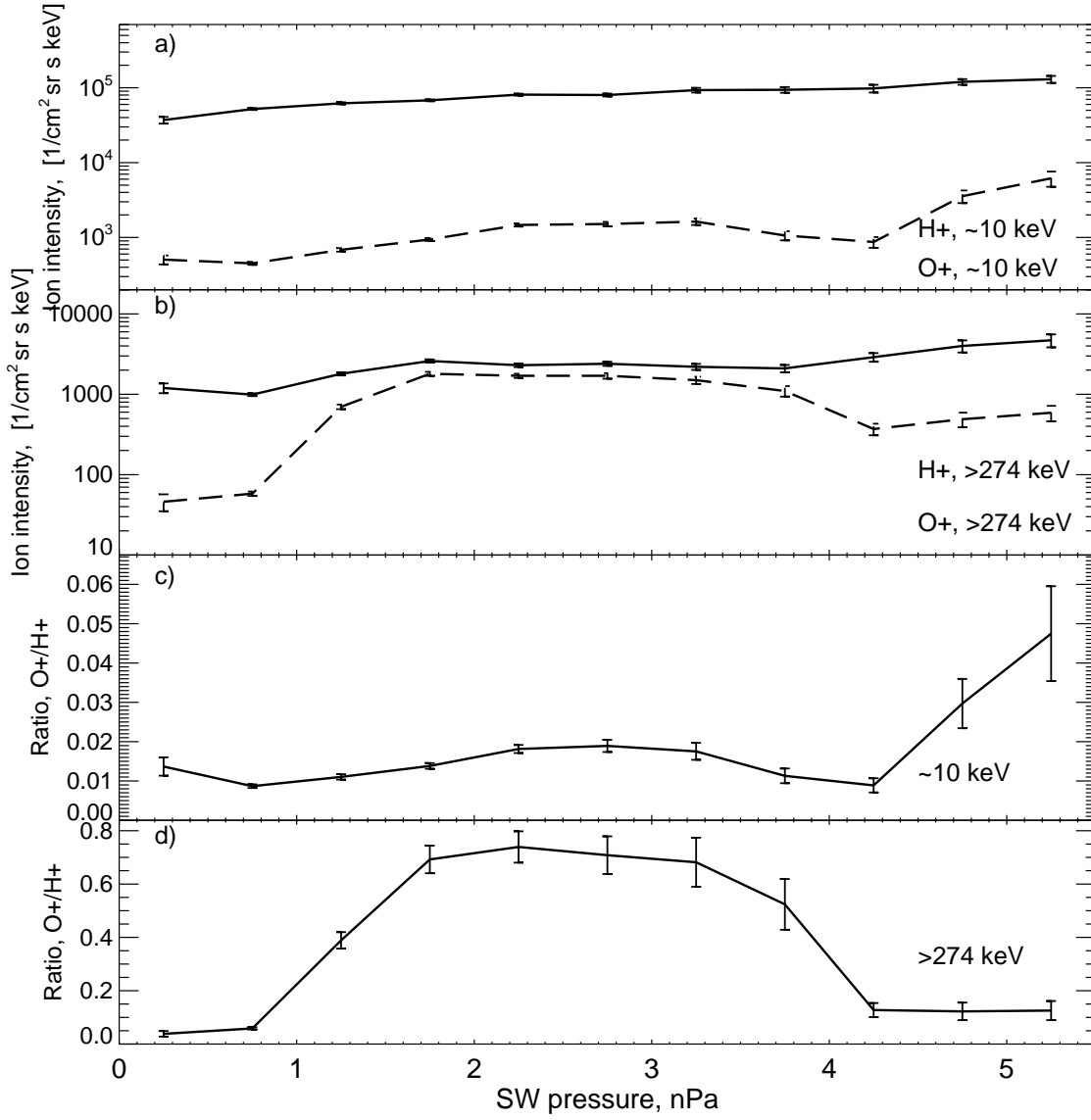


Figure 6. Dependencies on solar wind pressure of (a) proton and oxygen intensities at ~ 10 keV, (b) proton and oxygen intensities at >274 keV, (c) ratio O^+/H^+ for intensities at ~ 10 keV and (d) ratio O^+/H^+ for intensities at >274 keV.

Table 3. O^+/H^+ ratios of energy density depending on the disturbance level and the location.

Satellite, instrument	Energy range, keV	O^+/H^+ , Energy density	
		Quiet time	Disturbed time
Cluster/RAPID	274 keV - \sim 955 keV	0.22 ± 0.12^a , 0.72 ± 0.44^b	1.04 ± 1.33^a , 1.11 ± 1.35^b
Cluster/CIS	\sim 10 keV	0.038 ± 0.0081^a , 0.034 ± 0.0031^b	0.083 ± 0.038^a , 0.2 ± 0.12^b
AMPTE/CCE ^c	1-310 keV	0.03	0.34
AMPTE/CCE ^d	1-310 keV	0.01	0.61
Geotail/EPIC ^e	9-210 keV	0.05-0.1	0.2-0.6

^a Quiet ($AE < 100$ nT) and disturbed conditions ($AE > 300$ nT) are based on the AE index.

^b Quiet ($Dst \sim 0$ nT) and disturbed (Dst is between -100 and -30 nT) are determined based on the Dst index.

^c Measurements taken from *Gloeckler et al.* [1985].

^d Measurements taken from *Hamilton et al.* [1988].

^e Measurements taken from *Nosé et al.* [2001].

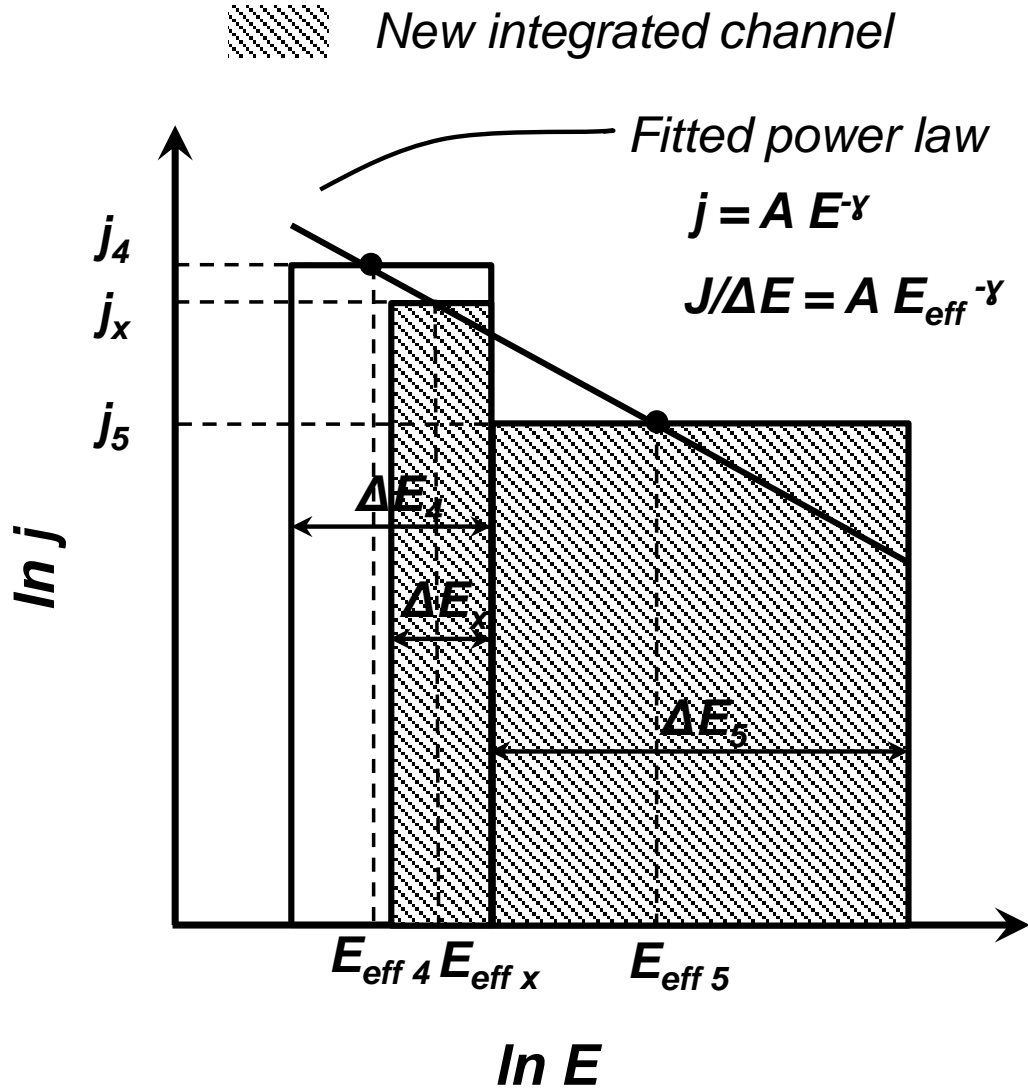


Figure 7. Bringing RAPID H⁺ channels to the same energy range as O⁺ channels: the differential flux in channels $E_4^{H^+}$ and $E_5^{H^+}$ is fitted to a power law, that fit is used to determine the differential flux, j_x , in the virtual channel E_x . E_{eff} is the energy at which the spectrum with given A and γ has the differential flux equal $J/\Delta E$, where J is the integrated intensity.